PAPER

Check for updates

Harnessing light in tandem: advanced erbium-polyaniline QD composites for next-generation energy storage

Marwa Ennouri,* Jan Svoboda, [iD] Zuzana Morávková, [iD] Jiřina Hromádková and Elena Tomsik [iD] *

Simultaneous harvesting of sunlight and storing its energy in optoelectronic devices is a scientific challenge. The current work pursues two main goals: (1) to understand the interaction of erbium ions with stable PANI quantum dots (QD, 8 nm), obtained by acid-assisted polymerization method, and (2) to investigate the potential application of Er-PANI:PSS composite as a next-generation energy storage system. PANI QD of 8 nm size is synthesized for the first time, stabilized by PSS and decorated with Er^{3+} ions. FTIR and XPS analyses confirm that no direct erbium-PANI coordination is observed; nevertheless, PANI is likely present in the second coordination sphere of the erbium complex, potentially enabling energy transfer between the PANI π-system and Er^{3+} ions. CV and LSV measurements show that the incorporation of Er^{3+} ions into the composite leads to a marked improvement in electrochemical performance. A further enhancement in areal current was achieved under light irradiation, particularly when using a 655 nm LED, which corresponds to one of the most intense regions of the solar spectrum. The enhanced photoelectrochemical activity is attributed to a synergistic mechanism involving photo-assisted PANI protonation and Er^{3+}-mediated charge storage, where Er^{3+} ions create new redox states and facilitate efficient outer-sphere electron transfer, stabilizing charge carriers and boosting photocurrent generation. These findings highlight the promise of Er-PANI:PSS composite for integrated solar energy harvesting and storage technologies.

Introduction

The dual challenges of mitigating industrial CO_2 emissions and satisfying the surging global energy demands, reaching approximately 30 000 TWh in 2024 with a significant 4.3% year-over-year increase,[1] are driving an accelerated transition toward renewable energy sources. Among these, solar energy is an incredibly powerful and practically inexhaustible source of clean energy, offering a theoretical energy potential that far exceeds current global consumption.[2] However, the intermittent nature of solar energy poses a significant challenge, as its output fluctuates based on weather conditions, leading to an inconsistent supply. To address this issue, the development of high-efficiency energy storage systems has become essential.

Over the years, efforts have explored the integration of charge storage devices, such as thin-film batteries or supercapacitors, directly with photovoltaic cells, establishing a foundational approach for combining solar energy conversion and storage within a single device. However, recent advancements have shifted focus toward developing unified systems that integrate light conversion and energy storage into a single architecture.[3] These next-generation designs prioritize seamless integration through shared electrode structures and minimized charge transfer distances to enhance overall system efficiency.[4,5] While photoelectrochemical (PEC) devices, such as solar fuel cells, can directly convert sunlight into chemical energy with promising efficiencies, their practical use is still limited by low energy density and slow reaction kinetics. However, their counterparts, such as redox flow batteries (RFBs), offer scalable storage solutions with high power density and function as passive systems incapable of directly harnessing solar energy. Achieving simultaneous high-density charge storage and photo-driven energy conversion within a single system could mark a significant step toward more effective and sustainable energy storage technologies. One promising way to combine these two functionalities is by using multifunctional materials exhibiting both light sensitivity and high electrochemical performance.[3]

Institute of Macromolecular Chemistry Czech Academy of Sciences, Heyrovského nám. 2, 162 00 Prague, Czech Republic. E-mail: ennouri@imc.cas.cz, tomsik@imc.cas.cz

In this context, electrochemically conducting polymers, like polyaniline (PANI) and its composites, are stepping into the spotlight.[6] They show promise with higher specific capacitance compared to traditional double-layer capacitors and faster charge-discharge kinetics than many inorganic batteries.[7–9] PANI, in particular, combines both a high theoretical charge storage capacity and a broad operational potential window that enables higher energy density.[10–12]

In our recent studies, PANI synthesized through acid-assisted polymerization forms stable suspensions that, when deposited on low-boron-doped diamond electrodes, achieved a specific capacitance of 958 F g^{-1}, reaching about 90% of its theoretical limit at a scan rate of 0.01 V s^{-1}.[13] Plus, it is easy to synthesize, cost-effective, and highly stable thermally and environmentally, making it ideal for applications requiring prolonged exposure to heat.[12]

Rare-earth (RE) elements are known for their unique electronic structure, which confers promising optical, electrical, magnetic, and catalytic features, making them indispensable in a wide range of advanced technologies.[14–17] Their potential in next-generation energy storage remains relatively underexplored, and it is only in recently that researchers have begun to recognize their potential in the field of pseudocapacitive energy storage.[18] RE-based redox flow batteries were also investigated in the last few years. In particular, RE-based RFBs have emerged as a promising alternative to conventional vanadium-based systems. D. Zeng et al.[19] introduced the first fully rare-earth-based RFB, showing superior voltage and performance, a finding supported by Yating Wu et al.[20] work, which reported an acidic Eu–Ce flow battery with an ultrahigh cell voltage, an impressive energy density and efficiencies. These studies highlight the potential of REs in sustainable, high-performance energy storage systems.

Among RE, erbium presents an interesting prospect as an electroactive material due to its rich redox chemistry and potential for high-capacity charge storage. Recent studies on ErCl$_3$ alkaline aqueous pseudocapacitors show that erbium can undergo one-electron ($Er^{3+} \rightleftharpoons Er^{2+}$), two-electron ($Er^{2+} \rightleftharpoons Er^{0}$), or even three-electron ($Er^{3+} \rightleftharpoons Er^{0}$) redox transitions, suggesting its versatility for high-capacity storage.[21] ErCl$_3$ alkaline pseudocapacitor electrodes formed from ErCl$_3$ salt in high-pH electrolytes have shown high-performance supercapacitor behavior.[21] Moreover, research on Er(OH)$_3$ or Er$_2$O$_3$ electrodes has revealed that nanometric cubic Er$_2$O$_3$ particles exhibit a high specific capacitance of 822.99 F g^{-1}, stable charge-discharge behavior, and favorable electrical conductivity.[22] Furthermore, Er-doped compounds have demonstrated enhanced charge transfer kinetics and improved electrode interface stability, further supporting their potential use in hybrid redox flow batteries.[23,24] Additionally, the unique optical properties of Er^{3+} open pathways for photo-assisted energy storage, where light absorption could contribute to improved redox reaction efficiencies. These findings indicate that erbium could serve as a valuable component in next-generation flow batteries, particularly in systems leveraging both electrochemical and photoelectrochemical

mechanisms to enhance energy conversion and storage performance.

Combining the features of these two components into only one composite will be of great interest for photoelectrochemical applications. Therefore, this study aims to develop a novel, stable composite material that leverages the light sensitivity of Er^{3+} and the electrochemical activity of PANI to achieve enhanced photoelectrochemical energy storage performance through improved light-driven energy conversion and charge storage efficiency.

Results and discussion

This study advances the development of erbium-containing polyaniline:polystyrene-sulfonate (Er-PANI:PSS) composite suspensions for enhanced photoelectrochemical energy harvesting and storage. Initially, an *in-situ* polymerization approach was attempted to incorporate erbium into the polymer backbone. However, impedance analysis indicated that this method yielded poor performance composites (Fig. S1), likely due to unfavorable electronic and ionic transport properties. Therefore, the study proceeded with a post-polymerization synthesis, involving the addition of Er-HCl solution to the pre-formed PANI:PSS solution, to localize erbium at the polymer surface and optimize interfacial interactions (Scheme 1).

In this method, PANI was first separately prepared *via* acid-assisted polymerization of aniline in the presence of concentrated formic acid (con. HCOOH) initiated by adding a very small amount of APS as an oxidant. After polymerization, a PSS solution was added to further stabilize PANI QD suspension during integration of erbium ions. In the final step, an equal volume of Er-HCl solution (Er-solution) was introduced to the PANI:PSS suspension to obtain the final composite, labelled as Er-PANI:PSS. Further details are provided in the experimental part.

Characterizing the photoelectrochemical energy storage performance of materials requires understanding their interaction with light. To this end, UV–Vis absorption spectra of the Er precursor solution, the PANI:PSS suspension, and the resulting Er-PANI:PSS composite suspension were measured and shown in Fig. 1a–c.

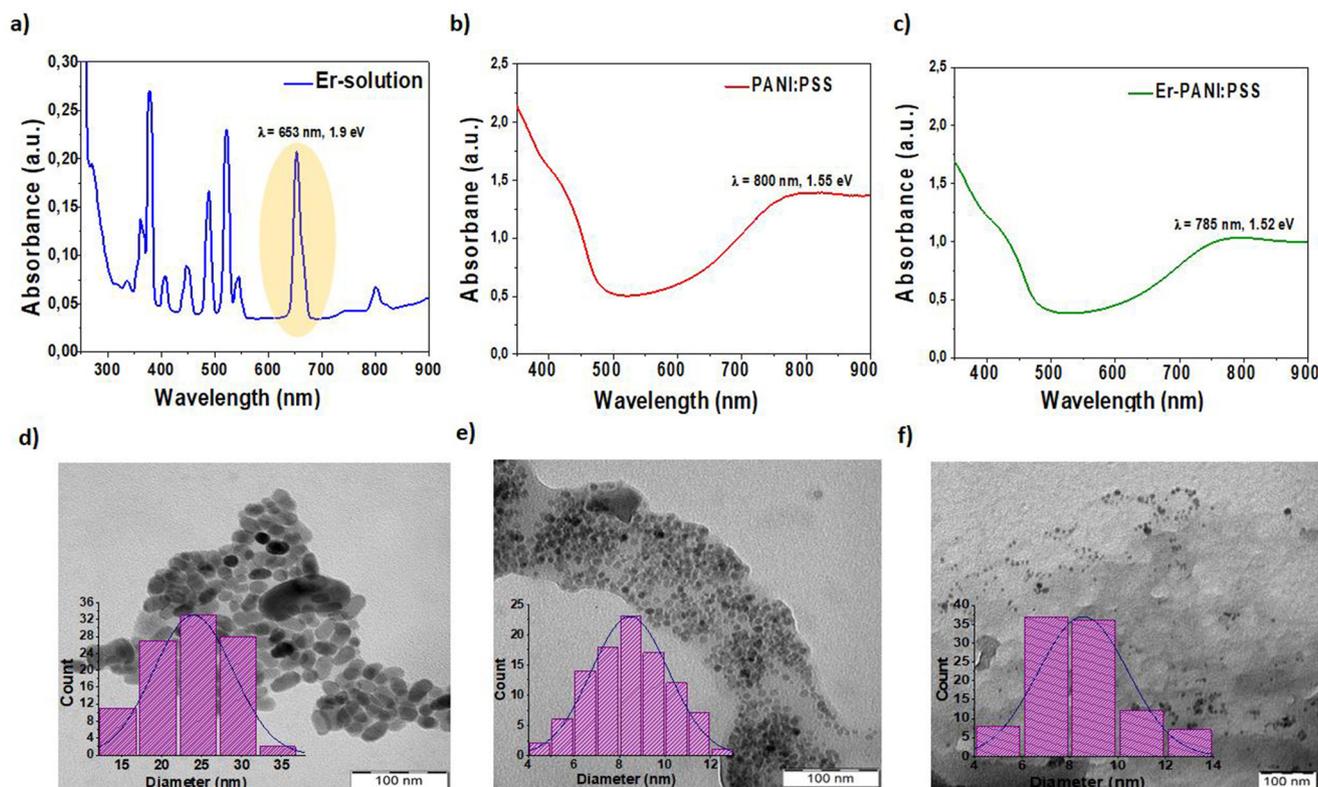**Scheme 1** Road map of composite suspension preparation: post-polymerization synthesis.

Fig. 1 UV-Vis absorption spectra of (a) Er–HCl, (b) PANI:PSS, and their corresponding composite suspension (c) Er–PANI:PSS and TEM image of (d) Er–HCl, (e) PANI:PSS, and their composite suspension (f) Er–PANI:PSS.

According to measured data (Fig. 1a), Er precursor solution displays distinct, well-defined absorption bands, linked to the intra-configurational f–f transitions within the $4f^{11}$ electron shell characteristic of the Er^{3+} ion, from its ground state $^4I_{15/2}$ to its different excited states. Conversely, PANI:PSS (Fig. 1a) possesses a broad and relatively high absorption across the visible and NIR ranges, characteristic of conjugated conducting polymers.[25,26] This absorption exhibits a dip in the green region, consistent with its observed dark green coloration. The PANI:PSS suspension displays two prominent absorption features. The first, observed at approximately 2.88 eV (430 nm), is attributed to the transition from polaron band to the π^* band. The second, a lower-energy band centred around 800 nm (1.55 eV), is associated with the complementary transitions from the ground state to the polaron state, and also linked to the extended conjugation of the polymer backbone.[27,28] Upon the introduction of Er-species into the PANI:PSS suspension, the UV–Vis spectrum of the resulting composite (Fig. 1c) closely resembles that of PANI:PSS, indicating that the polymer matrix dominates its optical response. The absence of discernible Er^{3+} characteristic absorption bands in the composite spectrum is attributed to the higher absorption coefficient of PANI, effectively masking any contributions from the incorporated Er^{3+} ions. However, the blue shift in both the lower energy absorption band to 1.58 eV and the visible absorption edge observed for the composite suspension connected with charge

polaron localization[29,30] or even partial coupling to bipolarons.[31] This can serve as indirect evidence of the interaction of Er^{3+} with the PANI:PSS systems, since Er^{3+} is not directly coordinated to the polymer backbone but is instead complexed *via* formate ligands, indicating an outer-sphere interaction, which will be studied in detail by FTIR. Studies on conducting polymers modified with outer-sphere metal complexes have reported that metal centres can perturb the energy levels of the polaronic and bipolaronic states, resulting in such spectral shift.[32] From the TEM images of the studied suspensions (Fig. 1d–f), the Er precursor solution exhibits the largest particle formation among the three samples, consisting of asymmetric ovoid-shaped nanoparticles with an average diameter of approximately 24 nm dispersed throughout the solution. In contrast, the TEM image of the as-prepared PANI:PSS suspension shows smaller particles with a roughly square shape, exhibiting quite homogeneous dispersion within the polymeric suspension. As previously reported in the literature on metal-doped polymers, the final suspension likely contains metal nanoparticles embedded or complexed within the polymeric network.[33,34] However, the mixed suspension predominantly reveals smaller features, approximately 8 nm in size, corresponding to PANI domains, while the larger Er-containing particles are not visible. This could be attributed to stronger chemical interaction between erbium and PSS compared to PANI (discussed further in the FTIR analysis). Such complexa-
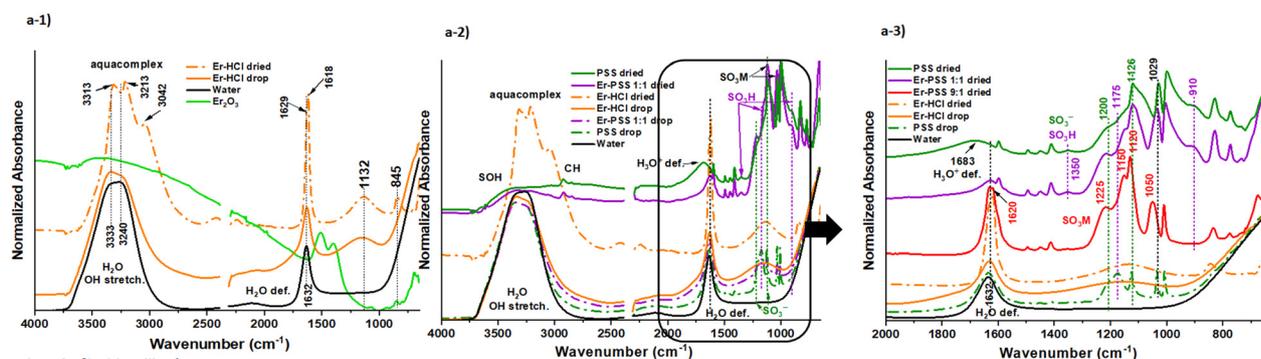
tion suggests that Er is no longer present as electron-dense nanoparticles but is instead tightly coordinated within the polymer matrix. In this case, the electron density difference between the Er–PSS complexes and the surrounding polymer is significantly reduced, diminishing the contrast in TEM signal. This reduced contrast makes it difficult to resolve the Er-containing particles clearly, making them invisible in the final suspension.[35] Despite the lack of clear visibility in TEM, the presence of erbium in the final composite suspension is confirmed by Energy-Dispersive X-ray Spectroscopy (EDX), which shows distinct spectral features indicative of Er species (as shown in the SI (Fig. S2)).
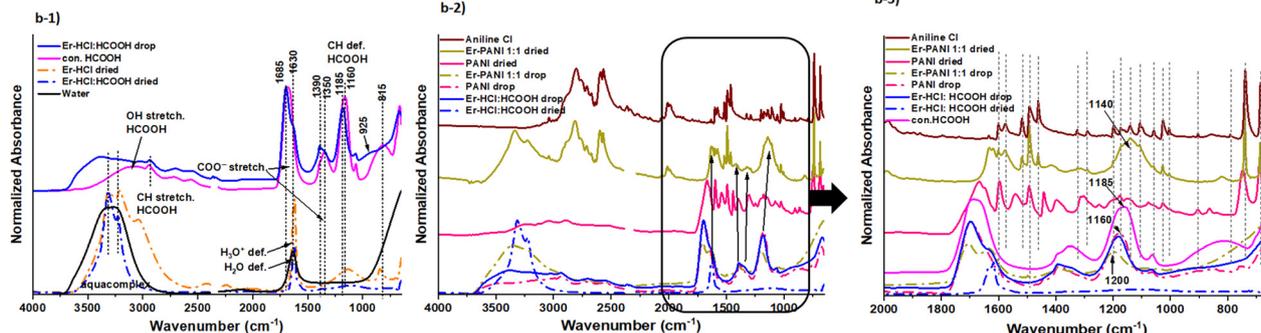
To investigate the interactions within the Er-PANI:PSS system, FTIR spectra of simplified binary suspensions consisting of Er-HCl : PSS (1 : 1 and 9 : 1 mass ratio of Er to PSS), Er: HCl–HCOOH, Er-HCl : PANI (1 : 1 mass ratio of Er to PANI) were first analyzed. Subsequently, the complete Er-PANI:PSS system was also studied. The FTIR spectra of each individual component and their respective combinations with the Er-solution are presented in Fig. 2

By analysing the spectra (Fig. 2a-1), it is seen that upon dissolving Er_2O_3 powder in HCl, the weak IR signals of the oxide (seen in Er_2O_3 powder) completely disappear, and a new band at 1140 cm^{-1} emerges compared to the spectrum of pure
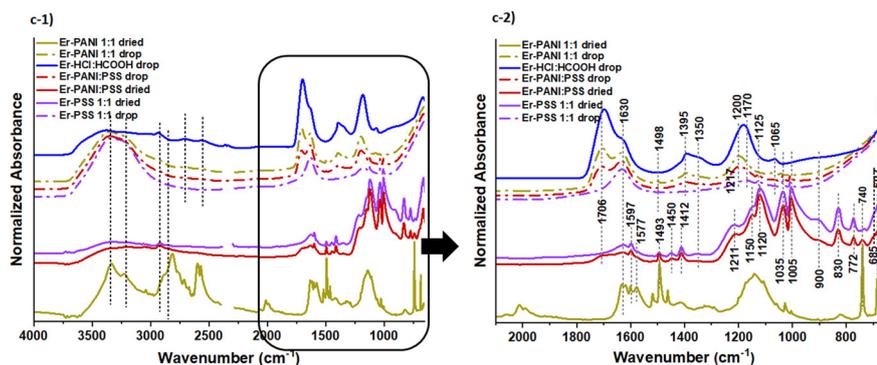

Fig. 2 FTIR spectra illustrating the interactions between erbium and the individual components of the system. (a-1) Spectra of erbium in hydrochloric acid (liquid and dried), with solid Er_2O_3 and water shown for comparison. (a-2 and a-3) Full range and fingerprint region of PSS with and without erbium, in both liquid and dried states, including erbium in HCl. (b-1) Spectra of formic acid solutions and dried samples, with reference spectra of water and dried erbium in HCl. (b-2 and b-3) Full range and fingerprint region of PANI colloids/suspensions, in both liquid and dried states, including spectra of solid aniline hydrochloride and erbium in HCl. (c-1 and c-2) Full range and fingerprint region of the final Er-PSS:PANI composite, highlighting the resulting coordination interactions.

water, indicating the formation of metal-aqua complexes.[36] Furthermore, the broadening and changes in the shape of the OH stretching and H_2O deformation bands provide additional evidence for the coordination of water molecules to Er^{3+} ions. Upon drying the solution, these broad bands split into several narrower bands, and a new band appears at 845 cm^{-1}. This suggests that the water molecules in the dried complex occupy more defined positions. The presence of bands at 3042 and 845 cm^{-1}, which are absent in the solution spectrum, indicates a change in the coordination environment around erbium and the formation of a different complex structure in the solid state compared to the solution. This transition aligns with the known ability of erbium to form ordered aqua-chloro-complexes,[37,38] where the dominant high-symmetry [Er(OH$_2$)$_9$]$^{3+}$ in acidic solution[39–41] likely transforms upon drying to a lower symmetry species [Er(OH$_2$)$_6$Cl$_2$]Cl (also described as ErCl$_3$·6H$_2$O).[42,43] In other words, Er^{3+} ions coordination shows an environment-dependent behavior, where chloride ions remain in outer solvation spheres in solution but become coordinated in the solid state.[40,41]

From the FTIR spectra of PSS (Fig. 2a-2), it can be perceived that the signal of PSS is rather strong in liquid drop, where strong peaks of SO$_3^-$ stretching bands at 1200 and 1126 cm^{-1}, SO$_3$H bands at 1350, 1175 and 910 cm^{-1}, and aromatic ring vibration bands at 1495, 1453, 1034, 1008 cm^{-1} (contributing also to bands at 1175 and 1125 cm^{-1}) are present[44] along the broadened water bands due to the higher content of H_3O^+. While the SO$_3^-$/H$_3$O$^+$ structure dominates the spectrum of the solution, after drying, features connected with SO$_3$H become more prominent, and all bands broaden as the solvation structure is lost. Upon adding Er-solution to PSS, the features of SO$_3^-$, H$_3$O$^+$, and SO$_3$H structures were replaced by a set of narrower bands at 1225, 1150, 1120, and 1050 cm^{-1} attributed to a sulfate metal salt (Fig. 2a-2 and 2a-3 red and violet lines).[44,46]

In addition, bands very similar but not identical to those of the [Er(OH$_2$)$_6$Cl$_2$]Cl complex at 3317, 3218, 3070, 1632, 1620, and 1120 cm^{-1} underlie the spectrum of PSS. These observations suggest that, in the dried sample, the sulfate anion enters the erbium solvation sphere and partially replaces the chloride ions. In solution, however, no change to the PSS FTIR features was detected; we assume that, similarly to chloride ions, the sulfate ions coordinate in the outer solvation sphere of the erbium ion.

To investigate the possible interactions between PANI and erbium species, the interaction of Er-HCl with concentrated formic acid (con. HCOOH) was first studied, as formic acid is part of the polymer matrix. Starting from the FTIR spectrum of concentrated formic acid (Fig. 2b-1), distinct vibrational bands are shown, including CH modes observed at 2945 cm^{-1} and 1160 cm^{-1}, bands attributed to water deformation and H$_3$O$^+$ bending vibrations at 1630 cm^{-1} and 1685 cm^{-1}, respectively. The COO$^-$-related bands include asymmetric stretching near 1660 cm^{-1}, which overlaps with the water deformation band, symmetric stretching at 1390 cm^{-1} and 1350 cm^{-1}, and deformation vibrations at 815 cm^{-1} are also observed.[44] Notably,

the C=O stretching band of non-dissociated COOH dimers is not resolved, indicating that the acid is fully dissociated. The spectrum of the dried sample could not be obtained, as formic acid evaporated along with water. After adding the Er-solution (Fig. 2b-1, blue line), the shape of the broad OH stretching band changed, and the water and H$_3$O$^+$ deformation bands became clearly resolved. The ratio between the two components of the HCOO$^-$ symmetric stretching bands also changed; the HCOO$^-$ deformation band transformed into a broad feature centered around 925 cm^{-1} and the CH deformation band shifted to 1185 cm^{-1}. These changes indicate a reorganization of the hydrogen-bonding structure in the formic acid solution. As a result, the formic acid molecules likely undergo a reconfiguration, coordinating with the erbium aquacomplex. After drying (Fig. 2b-1, blue dashed line), the formic acid-related bands practically disappear due to evaporation. However, the resulting spectrum differs from that of Er in HCl (Fig. 2b-1, orange dashed line), retaining characteristic markers of aqua complexes. A possible explanation for these changes is that formic acid transiently enters the Er^{3+} coordination sphere as a bidentate ligand in solution. This behavior is supported by previous reports on complexes of erbium with ketones[43,47] and carboxylic acids,[46,48] in which the carbonyl group directly coordinates to erbium in the first solvation sphere; it is thus a stronger ligand for erbium than the chloride ions. On drying, formic acid evaporates, and another ligand, likely water or chloride, replaces it in the complex. These findings highlight the dynamic ligand exchange behavior around Er^{3+} ions in response to changes in the chemical environment.

The FTIR spectra of PANI-containing solutions (Fig. 2b-2 and 2b-3) are primarily dominated by formic acid and water bands. In the spectrum Er-HCl : PANI 1 : 1 solution, clear splitting to H$_2$O and H$_3$O$^+$ deformation is observed, pointing to the presence of erbium aquacomplex [Er(OH$_2$)$_8$]$^{3+}$ typical in highly acidic medium. After drying, the PANI spectrum deviates from the standard PANI structure,[49,50] indicating a distinct molecular configuration due to low oxidant concentration, which will be the subject of future investigations. The addition of Er-solution significantly alters the spectrum, revealing bands associated with formic acid, [Er(OH$_2$)$_9$]$^{3+}$, and aniline hydrochloride. While direct coordination between PANI and Er was not detected, PANI interacts with HCl, disrupting its molecular and supramolecular structure. In samples containing PANI, erbium, and formic acid, the formate CH deformation band shifts to 1200 cm^{-1}. This shift indicates that formate anions enter the coordination shell of erbium and become detached from PANI. Subsequently, upon drying, this band shifts in the opposite direction to 1140 cm^{-1}. It appears that the presence of PANI hinders the evaporation of formic acid from the erbium complex. As unbound water evaporates and PANI (or its residual components) crystallizes with chloride ions, there are fewer available H-bond acceptors. Consequently, the band at 1140 cm^{-1} is assigned to the formate CH stretching free of H-bonds. The erbium complex is detected in the dried PANI colloid with erbium by the OH stretching fingerprint, and the

observed maxima relate to a complex with formate anions and water as ligands. However, in practical systems, the low Er-HCl content relative to PANI minimizes this destructive effect, which is supported by the observed suspension stability. In liquid samples, Er coordinates with water, PSS, formic acid, and chlorides; with PSS and formic acid being closely intertwined with PANI, further supporting the suspension stability and electrochemical properties. Direct coordination of PANI to Er is not observed, even though the nitrogen atoms in PANI could theoretically enter the erbium coordination sphere, as erbium complexes with nitrogen-containing aromatic compounds have been reported.[45–47,51,52]

In the FTIR spectra of the full system (Fig. 2c-1 and 2), the PANI component is not clearly detected; the spectra mainly reflect the acids. Only the increase of bands at 1493, 740 cm^{-1} and a weak shoulder at 685 cm^{-1} suggests its presence in the dried state. The spectrum in the wet state primarily reflects the acids component. In the presence of PANI, the carboxylic acid C=O stretching shifts to 1706 cm^{-1}, indicating the transition from COO$^-$ to COOH as formic acid protonates PANI and forms a H-bond with the NH$^+$ of PANI. Upon adding PSS, this band decreases (relative to the water molecule deformation band at 1630 cm^{-1}), as PANI is partially protonated by PSS instead of formic acid. The ratio of the two maxima associated with COO$^-$ group symmetrical stretching at 1395 and 1350 cm^{-1} changes; the maximum at 1350 cm^{-1} decreases in the presence of PANI and becomes undetectable in the full system. The rocking vibration of water in the erbium aquacomplex is observed around 1200 cm^{-1} with a shoulder at 1170 cm^{-1}. Both these maxima are seen in the erbium solutions with PSS, although with a reversed height ratio, and the 1200 cm^{-1} maximum dominates this region of the Er-PANI solution spectrum. This suggests that erbium is coordinated with both formic acid and PSS in its second coordination sphere. PSS is indicated by bands at 1125, 1035, and 1005 cm^{-1}. In the dried state, the FTIR spectra mainly show the PSS component, as water and formic acid largely evaporate. Residual formic acid is

observed through the C=O stretching band at 1706 cm^{-1}, suggesting that formic acid molecules protonating PANI are stabilized by the presence of PSS. Water produces only a small maximum around 1630 cm^{-1}. PSS bands are mostly at similar positions as in the Er-PSS solutions, except for the SO$_3^-$···M$^+$ band, which shifts from 1217 to 1211 cm^{-1} upon PANI addition. This shift is expected, as PANI also acts as a counter ion to PSS, and sulfate ion vibrations are sensitive to the specific cation.

Apart from water, erbium also shows possible interactions with PSS and formic acid, forming a complex ligand structure that maintains erbium ions in proximity to PANI. While direct coordination to PANI is not confirmed, it cannot be excluded. PSS and formic acid appear to be closely intertwined with PANI, consistent with the suspension's stability and electrochemical properties. Even without direct erbium-PANI coordination, PANI is likely in the second coordination layer, potentially enabling energy transfer between the PANI π-system and erbium.[46]

To get a better understanding of the interaction between the different compounds within the composite material, high-resolution X-ray photoelectron spectroscopy (XPS) was conducted. The deconvoluted spectra of the C 1s, N 1s, and Cl 2p, S 2p and Er 4d regions are shown in Fig. 3.

All XPS C 1s spectra (Fig. 3a) of the investigated suspensions were fitted with two main contributions; a dominant peak at 284.9 eV, assigned to the C–C bonds, and a small higher binding energy tail at 286.8 eV, corresponding to the C–N bonding.[53,54] The increased intensity of the C–N signal in Er-PANI (1 : 1) compared to PANI:PSS and Er-PANI:PSS could be explained by the fact that the interaction between erbium and formic acid likely resulted in the formation of erbium-formate complexes, which disrupt the H-bonding network between formate and PANI nitrogen atoms (as confirmed by the FTIR analysis). This weakening of interactions leads to a partial breakdown of the PANI supramolecular structure, releasing aniline units that subsequently crystallize with chloride ions to form aniline hydrochloride upon drying (FTIR evi-
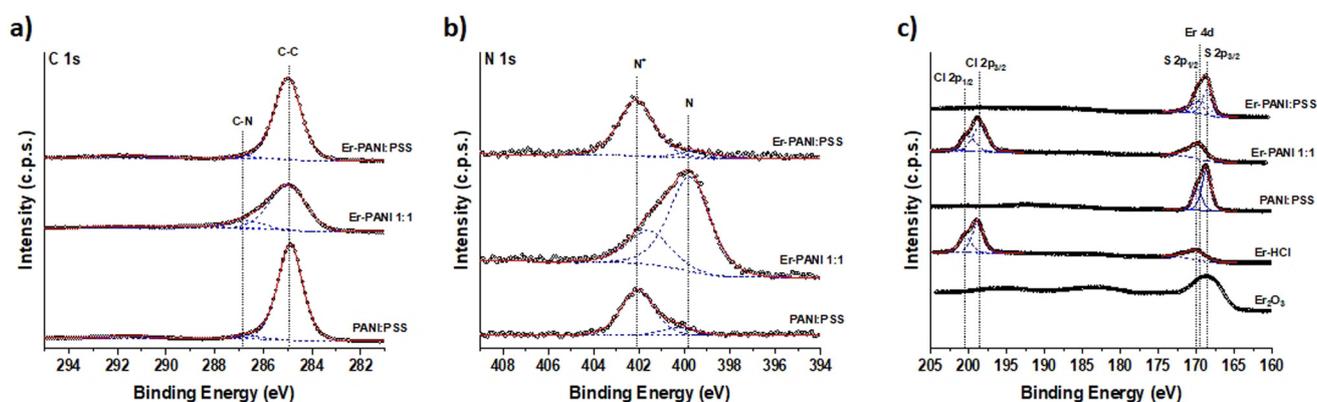

Fig. 3 High-resolution XPS core-level spectra of drop-cast films from PANI:PSS, Er-PANI, and Er-PANI-PSS suspensions: (a) C 1s, (b) N 1s, and (c) Cl 2p, S 2p, and Er 4d regions with reference spectra from Er-HCl and Er$_2$O$_3$. Survey spectra are available in the Fig. S3.

dence). This coordination increases the relative abundance of C–N environments, and thereby leading to a greater contribution in the XPS spectra.

For all the polymer suspensions, the N 1s spectra (Fig. 3b) exhibit two main contributions: one at ~399.8 eV related to nitrogen (N) species, including –NH– benzenoid amines (398.0–398.5 eV) and –N= quinoid imines (399.3–399.5 eV), and another at ~402.0 eV attributed to positively charged nitrogen (N$^+$) species (–NH$^{•+}$ and =NH$^+$).[55] The spectra of the samples containing PSS show a stronger N$^+$ contribution and only a minor presence of –N= groups, as indicated by a symmetric N$^+$ band with a small shoulder near 399.8 eV. As expected, the spectrum of Er-PANI (1 : 1) reveals a more electron-rich environment, characterized by a reduced N$^+$ signal and a shift toward lower binding energies, meaning an increased amount of –NH– benzenoid amines (here –NH– benzenoid amines (398.0–398.5 eV) become detectable). Typically, the ratio of positively charged nitrogen to neutral nitrogen species (N$^+$/N) reflects either the doping efficiency of the polymer or the charge stabilization. Notably, adding PSS the polymer suspensions results in a higher N$^+$/N ratio, with the absence of imine groups (=N–) suggesting complete protonation.[56]

The spectral overlap between Er 4d and S 2p core-level regions presented analytical challenges. However, by analysing the Er 4d/S 2p spectra across all samples (Fig. 3c), we found no evidence of metallic Er^0 (which typically appears between 167.5 and 167.7 eV). Instead, two peaks at 168.3 eV and 170.5 eV, associated with Er 4d$_{5/2}$, were observed, confirming that erbium is present in the +III oxidation state in all the investigated samples.[57,58] Compared to the spectrum of Er$_2$O$_3$ powder, the spectrum of Er$_2$O$_3$ diluted in HCl exhibits a shift to higher binding energy. The reduction in binding energy observed in the Er-PANI suspension compared to the precursor Er-HCl solution can be attributed to two main mechanisms. First, the formic acid (HCOOH) used during PANI preparation may act as a bidentate ligand, as supported by FTIR data. This would alter the first coordination sphere of Er^{3+} by replacing Cl$^-$ with HCOO$^-$. Since HCOO$^-$ is a stronger field ligand than Cl$^-$, it increases the electron density at the Er^{3+} centre through ligand-to-metal charge transfer, leading to a negative shift in binding energy observed in the XPS analysis. Second, protonated PANI chains (especially –NH$^+$= groups) may participate in second coordination with Er^{3+}, a possibility that is not excluded by FTIR analysis, contributing to electron-rich environments through π-conjugation effects.[59,60] The absence of the Cl 2p signal in the XPS spectrum of the Er-PANI:PSS sample is likely due to the weak retention of chloride ions within the polymer matrix, particularly in the presence of PSS. This interpretation is supported by FTIR analysis, which indicates that during drying, sulfate anions from PSS strongly compete with chloride ions for coordination sites around the Er^{3+} centers. As water evaporates, sulfate anions replace chloride in the erbium coordination sphere, forming stable Er-sulfate complexes. Meanwhile, chloride ions that are not strongly

bound to the matrix readily evaporate under the high-vacuum conditions of XPS analysis, resulting in their absence from the final spectrum.

The electrochemical characterization of the stable composite suspensions was done mainly by using cyclic voltammetry (CV) measurements. 3rd cycle CV curves of the as-prepared suspensions measured using a three-electrode cell configuration within the potential window of [−0.3 to 0.8] V vs. Ag/AgCl at a scan rate of 5 mV s^{-1}, are presented in Fig. 4.

The CV curve of Er-solution exhibits significantly lower current density compared to PANI:PSS (~10× reduction in magnitude), a discernible reduction peak at 0.3 V vs. Ag/AgCl confirms the electroactivity of the Er-solution (Fig. 4a). This feature is probably attributed to the one-electron reduction of Er^{3+} to Er^{2+}. Interestingly, by simply introducing Er-solution into the PANI:PSS suspension, an important improvement in the overall current density of the suspension is shown, especially for the reduction current (Fig. 4c), which increases by more than three times compared to the original PANI:PSS solution (Fig. 4c). This enhancement is particularly intriguing given that the total volume of the suspension remains unchanged, meaning a proportional decrease in PANI concentration compared to the pristine PANI:PSS. This result highlights a unique interaction between Er^{3+} ions and the other compounds of the system that significantly enhances the electrochemical performance of the composite, suggesting potential synergistic effects that warrant further investigation. The photoelectrochemical technique provides insights into the electrochemical behavior of the material under light irradiation. The photoelectrochemical activity of the investigated suspensions was studied via CV measurements on a 3-electrode cell configuration using FTO as the working electrode, Pt wire as the counter electrode, and Ag/AgCl as the reference electrode. Two LED light sources were used: blue (470 nm) and deep-red (655 nm) lights. Based on the CV data of the Er precursor solution recorded under different light illuminations (Fig. 4d), the reduction current increases upon light exposure. In agreement with the Er-solution absorption spectrum, the more photons the system absorbs, the more pronounced its impact on the CV data. For instance, when irradiated with 470 nm light, a slight increase in the reduction current was observed, which became more significant with 655 nm irradiation. According to the UV-Vis data (Fig. 1a), Er^{3+} exhibits a distinct absorption band precisely at 655 nm, while it absorbs about 2 times less at 470 nm. Greater light absorption at a specific wavelength generates more excited electrons, resulting in a proportional increase in photocurrent under illumination at that wavelength.

In addition to the Er-solution, the PANI:PSS suspension also demonstrates improved behavior under light irradiation. It is published in the literature that PANI has photocurrent, but in the current work the increase of the current under light irradiation was 14 times for 655 nm LED and 26 times for 470 nm LED (from 0.25 mA cm^{-2} to 3.5 mA cm^{-2} and 6.5 mA cm^{-2} correspondingly), which is explained by the size
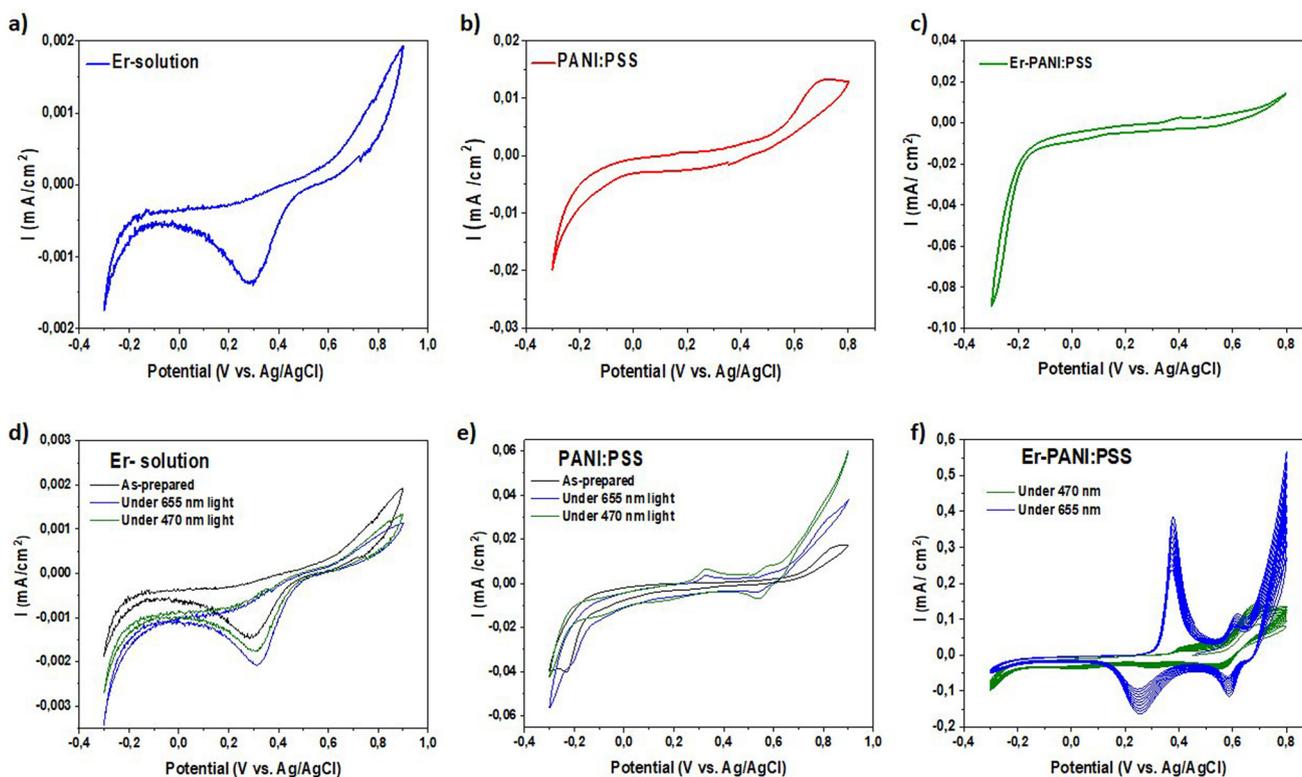
Fig. 4 CV curves of as-prepared (a) Er-solution, (b) PANI:PSS, and (c) Er-PANI:PSS composite. CV curves under different light irradiations (red and blue) of (d) Er-solution, (e) PANI:PSS, and (f) Er-PANI:PSS suspensions. The evolution of the peak current of Er-PANI:PSS under both blue and red light is shown in Fig. S3.

of the PANI QDs – 8 nm (Fig. 1b). Moreover, this effect is more pronounced when erbium is added to the final solution. The irradiated Er-PANI:PSS suspension exhibited a current that was 10 times higher, with more pronounced oxidation/reduction peaks, after several cycles of measurement (30 cycles in total).

By comparing the effects of the two irradiation wavelengths used in this study, we concluded that 655 nm irradiation had the most significant influence on the electrical performance of our composite, as indicated by the evolution of peak current over time (Fig. S4). Analysis of the photocurrent response revealed a linear increase over time, with the curve exhibiting a steeper slope under 655 nm irradiation compared to the alternate wavelength. This indicates an efficient generation and extraction of charge carriers under 655 nm illumination, which is consistent with what was observed in the Er-solution, suggesting a significant contribution of Er^{3+} to the observed photoelectrical enhancement. That is why, further electrochemical characterization was done only under 655 nm irradiation.

In addition to the increased photocurrent, CV curves exhibited a shift of the peak current toward lower potentials, accompanied by the emergence of new oxidation/reduction events. This behavior is more likely due to the interaction of Er^{3+} with the other compound of the system, mediating new energy states within the material. These states act as inter-

mediate energy levels, facilitating charge transfer processes and lowering the activation energy required for redox reactions. The presence of Er^{3+} ions can modify the electronic structure of the material, creating new pathways for electron transfer and enhancing the overall electrochemical activity. This is particularly evident in the emergence of new ox/red events, which indicate the formation of additional redox-active species or the stabilization of intermediate states during the electrochemical process, which is supported by the obtained FTIR data. Based on the FTIR spectra analysis, while erbium is not directly coordinated to PANI, it is present in the second coordination sphere of PANI, mediated by PSS and/or formic acid. This structural arrangement aligns well with the principles of Marcus theory,[61] which describes electron transfer as feasible even in the absence of direct bonding, provided there is sufficient electronic coupling through the surrounding medium. According to Marcus theory,[61] such outer-sphere mechanisms are facilitated by the proximity of donor and acceptor species and the reorganization of the solvent and ligands. The observed FTIR changes in hydrogen bonding provide direct molecular evidence for the dynamic interactions and reorganization processes that are fundamental to energy transfer. In the context of Marcus theory, these structural adjustments represent the reorganization energy required for electron transfer, as the local environment around the donor (PANI) and acceptor (Er^{3+}) evolves electronic and geometric

realignments of the system to lower the activation barrier for outer-sphere electron transfer.

The CV analysis of PANI:PSS (Fig. 5a) and Er-PANI:PSS over 30 cycles (Fig. 5b) reveals light-dependent electrochemical behavior. The as-prepared suspensions display the typical redox peaks of PANI, with the leucoemeraldine to emeraldine transition appearing around 0.15 V, and the emeraldine to pernigraniline transition around 0.43 V by the final cycle.[62] In the Er-containing suspensions, an additional pair of redox features emerges, showing a reduction peak ranging from approximately 0.53 to 0.64 V vs. Ag/AgCl and an oxidation peak near 0.73 V vs. Ag/AgCl. These features are absent in the pure PANI:PSS system, suggesting that the incorporation of Er introduces or facilitates additional redox processes, potentially related to the electroactivity of Er species or their interaction with the PANI:PSS matrix. Under red light irradiation (λ = 655 nm), the suspensions show a progressive increase in current, with a more pronounced
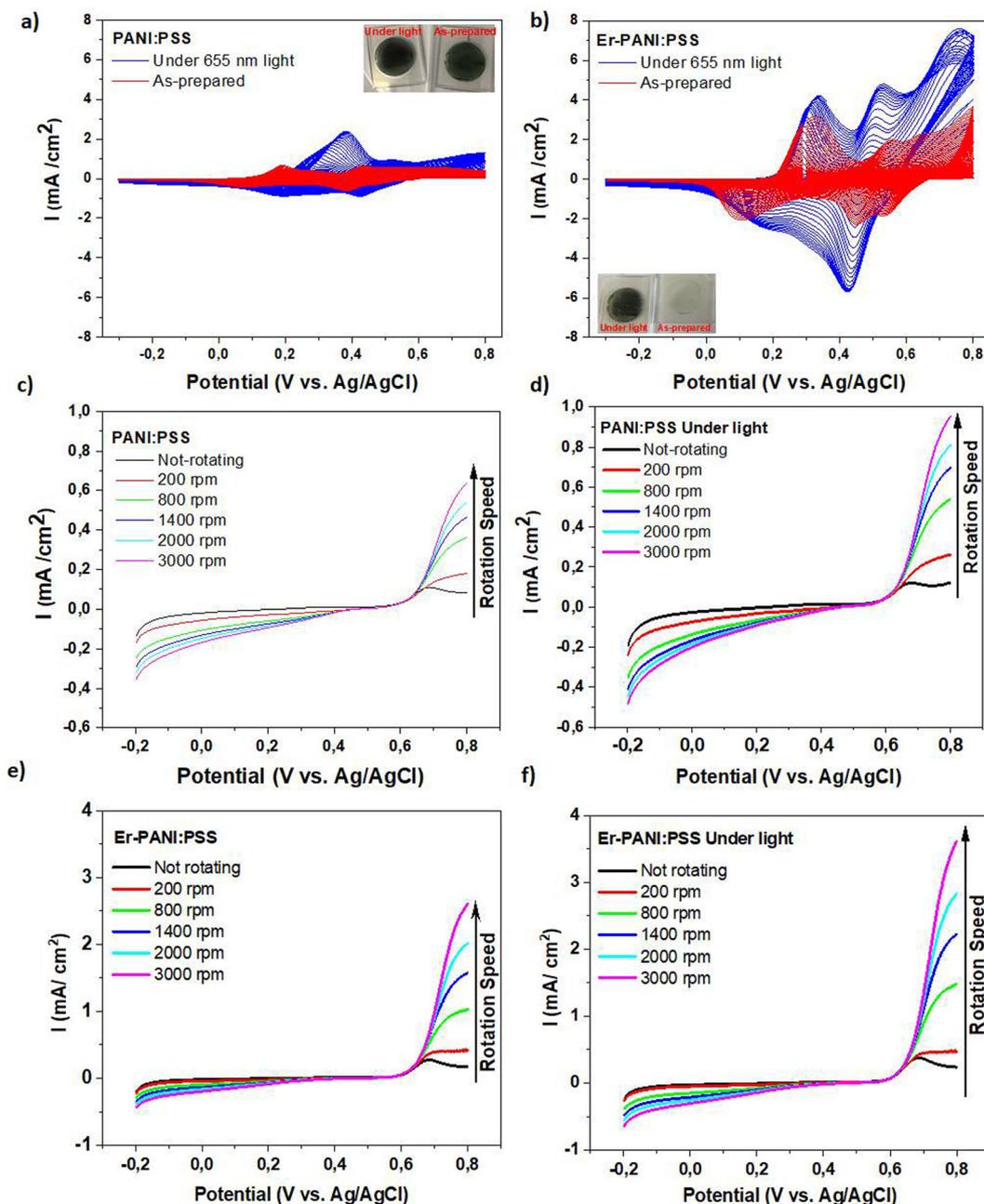

Fig. 5   CV curves of (a) PANI:PSS and (b) Er-PANI:PSS suspensions, measured in the dark and under 655 nm light irradiation. LSV curves of (c) PANI:PSS without light irradiation, (d) PANI:PSS under light irradiation, (e) Er-PANI:PSS suspensions without light irradiation, and (f) Er-PANI:PSS under light irradiation recorded using a rotating disk electrode (RDE).

effect observed in the Er-containing suspensions. By the final cycle, the current density of the Er-PANI:PSS suspension is 30 times higher than that of the as-prepared suspension. This current amplification is driven by two synergistic mechanisms: (i) photo-assisted protonation of PANI's emeraldine salt phase, which occurs in both suspensions and leads to an increase in polaron density and improved charge transport efficiency, and (ii) Er^{3+}-mediated charge storage, which is specific to the Er-containing suspension. In this process, Er^{3+} ions act as redox mediators, facilitating interfacial electron transfer and stabilizing charge carriers, which reduces recombination losses and enhances photocurrent generation. As a result of the irradiation, more electron-hole pairs are generated within the composite suspension, with Er^{3+} ions acting as electron traps to further enhance redox activity. These mechanisms further support the linear increase in photocurrent over time, which indicates more stable and consistent charge generation and extraction. The combination of enhanced light absorption, improved charge carrier dynamics, and modified electrochemical behavior highlights the critical role of Er^{3+} in the observed photoelectrochemical enhancement.

In the dark, a moderate increase in current is also observed for both suspensions, counted as about a 50 times increase in the integral area under CV curves for the PANI:PSS suspension and a 100 times increase in the presence of Er^{3+} in the suspension. During measurements, both systems develop a film at the working electrode surface, whose thickness increases upon exposure to irradiation, inducing a higher current. The observed enhancement in current, even without irradiation, can be attributed to improved mass transport, where a greater amount of electroactive material accumulates at the electrode surface, thereby facilitating more efficient electrochemical reactions. It is worth noting that this deposited material is not a permanently adhered film, nor is it the result of chemical reactions that cause radical-induced crosslinking. Instead, it remains in a dynamic equilibrium with the suspension and immediately dissolves back into the suspension upon immersion. The SEM images of the deposited films, as shown in SI (Fig. S5), further support the idea that the increase in current is associated with the accumulation of more material at the electrode surface or the formation of a thicker layer near the electrode surface. Specifically, the films formed from the as-prepared suspensions (both with and without Er^{3+}) exhibit relatively smooth surface morphology. In contrast, the films developed after light irradiation display more complex, accumulative, and porous surface structures. Based on EDX analysis coupled with these images (Fig. S5), the newly formed films contain the main compounds present in the system, including carbon, oxygen, as well as chlorine, and erbium in the Er-PANI:PSS suspension, except for nitrogen, which could be below the detection limit of the instrument. EDX analyses reveal increased amounts of both carbon and chlorine under light irradiation. The observed increase in carbon content and the detection of chlorine signal at the electrode surface in irradiated electrolyte can be explained through a photoinduced chlorine radical (Cl^-) generation mechanism mediated by erbium (III+) chloride complexes. Analogous to cerium-based photocatalytic systems, Er^{3+} chloride likely undergoes ligand-to-metal charge transfer under irradiation, facilitating homolytic cleavage of Er–Cl bonds to produce Cl^- radicals while reducing erbium to a lower oxidation state (Er^{2+}). These chlorine radicals initiate hydrogen atom transfer (HAT) from polymer C–H bonds, generating carbon-centred radicals.[63]

The second main objective of the current work is to investigate the prepared Er-PANI:PSS suspension as a promising cathode material for RFB systems.[64,65] To simulate the operational conditions of an RFB, linear sweep voltammetry (LSV) measurements were performed using a rotating disk electrode (RDE) configuration (Fig. 5c–f). In this setup, the electrode rotation mimics the dynamic electrolyte flow characteristic of RFB system, allowing us to evaluate the suspension's electrochemical behaviour under flow-like conditions. LSV experiments were performed both in the dark and under 655 nm light irradiation using a glassy carbon rotating disk electrode. Measurements were conducted at varying rotation speeds ranging from 200 to 3000 rpm to evaluate mass-transport-limited current, with a fixed scan rate of 5 mV s^{-1}. During the LSV measurements of PANI:PSS suspension and Er-PANI:PSS suspension, the potential was varied from the −0.2 V vs. Ag/AgCl to 0.8 V vs. Ag/AgCl. It is obvious from the graph that addition of Er^{3+} ions leads to the increase of the current density from 0.6 mA cm^{-2} for PANI:PSS at 3000 rpm to 2.5 mA cm^{-2} for Er-PANI:PSS (Fig. 5c and e). However, the half-wave potential is similar for both systems and it is 0.71 V vs. Ag/AgCl. Fig. 5d and f present the LSV polarization curves of the PANI:PSS and Er-PANI:PSS under 655 nm light irradiation, respectively. The obvious change of the current density is recorded for the PANI:PSS and Er-PANI:PSS under light irradiation. The current density increased from 0.6 mA cm^{-2} for PANI:PSS at 3000 rpm to 0.9 mA cm^{-2} at 3000 rpm under light irradiation, and from 2.5 mA cm^{-2} for Er-PANI:PSS at 3000 rpm to 3.75 mA cm^{-2} under light irradiation (1.5 time enhancement of the current). For all systems, the current density was increasing with the rotating speed, indicating the applicability of the synthesized system for RFB. The dependence of the limiting current vs. square root of rotating speed is presented in the Fig. S6. The linear dependences are observed for all investigated parameters. The electrochemical impedance spectroscopy (EIS), measured at open-circuit potential and frequency range from 100 kHz to 0.1 Hz, for PANI:PSS and Er-PANI:PSS without light and under light irradiation are recorded and presented in Fig. 6.

The corresponding equivalent circuit models for each system was developed and summarized in Table 1. The EIS is a powerful tool to explore ease of electron or ion flow at the interface, double-layer or faradaic capacitances, and other processes taking place at different frequencies. The Nyquist plots
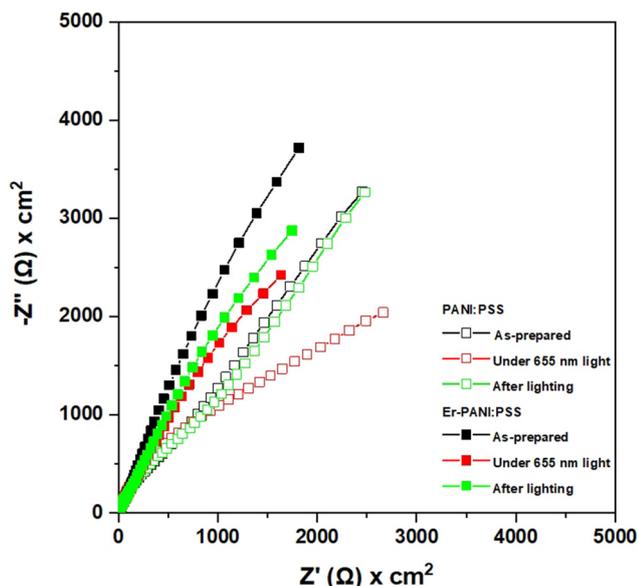
Fig. 6 Nyquist plots of EIS measured at room temperature of the investigated suspensions.

of PANI:PSS without light and after light irradiation are similar, however EIS curve of PANI:PSS under light irradiation increase its real part of the impedance with the simultaneous decrease of the imaginary one, which can be caused by inhomogeneity and porosity of the composite material and its interface, and can be simulated by the Constant Phase Element (CPE), Table 1. It is interesting to note that EIS of PANI:PSS under light irradiation has Warburg impedance lower compared to PANI:PSS without light. This means that

under light irradiation the studied system became less resistant for ions diffusion. Also, the capacitance of the double-layer increased for the measurement performed under light irradiation. The Nyquist plots of Er-PANI:PSS composite under different conditions improved their total impedance compared to data for samples without erbium (Fig. 6). Due to the presence of erbium ions in the final composite systems, it was decided to model the EIS measurements with circuit that has in series connected Resistance associated with charge transfer resistance (Table 1). It also interesting that the value of the Capacitance of double-layer part is 10 times higher for the composite with erbium compared to the one without. The value of the CPE for the measurement performed under light irradiation is 47.7 μMho*s, 39.2 μMho s without light, and 40 μMho*s after light irradiation. The χ^2 value is for all suggested models are presented in Table 1, also the corresponding equivalent circuit fitting curves are shown in Fig. S7.

The general conclusion from EIS data measurements before, under, and after light irradiation is that total impedance is improved under light irradiation, but the process is reversible.

A key parameter in energy saving materials is capacitance.

This study developed and characterized Er-PANI:PSS stable suspension for RFB. The areal capacitance was calculated from the CV measurements without and under light irradiation for PANI:PSS and Er-PANI:PSS. The areal capacitance of PANI:PSS is 47.2 mF cm^{-2} increased to 87.5 mF cm^{-2} under light irradiation (Fig. S8). Further improvement of areal capacitance was achieved by erbium ions and was 183 mF cm^{-2} without light. The areal capacitance of 299 mF cm^{-2} was measured for Er-PANI:PSS under light irradiation.

Table 1 Equivalent circuit fitting models and χ^2 values for PANI:PSS and Er-PANI:PSS suspensions in dark, under illumination, and after light exposure

Sample	PANI:PSS		
Equivalent circuit	As-prepared	Under light	After light irradiation
	R_s = 12.6 Ω, C_{dl} = 1.9 μF, $W(Y_o)$ = 25 μMho*s$^{0.5}$, C_{fr} = 160 μF	R_s = 10.1 Ω, C_{dl} = 2.8 μF, $W(Y_o)$ = 223μMho*s$^{0.5}$, CPE (Y_o) = 1.4 μMho*s (N = 0.419)	R_s = 13.9 Ω, C_{dl} = 1.6 μF, $W(Y_o)$ = 24 μMho*s$^{0.5}$, C_{fr} = 184 μF
χ^2	0.546	0.679	0.909
Sample	Er-PANI:PSS		
Equivalent circuit	As-prepared	Under light	After light irradiation
	R_s = 19 Ω, C_{dl} = 14.1 μF, $W(Y_o)$ = 13 μMho*s$^{0.5}$, CPE (Y_o) = 39.2 μMho*s (N = 0.75), R_{fr} = 2.02 kΩ	R_s = 16.4 Ω, C_{dl} = 15.3 μF, $W(Y_o)$ = 22.4 μMho*s$^{0.5}$, CPE (Y_o) = 47.7 μMho*s (N = 0.75), R_{fr} = 2.1 kΩ	R_s = 16.7 Ω, C_{dl} = 15.2 μF, $W(Y_o)$ = 18.2 μMho*s$^{0.5}$, CPE (Y_o) = 40 μMho*s (N = 0.75), R_{fr} = 2.02 kΩ
χ^2	0.133	0.136	0.136

Conclusions

In this study, stable suspensions of Er-PANI:PSS composites were successfully synthesized *via* a post-polymerization method, demonstrating significantly enhanced photoelectrochemical energy harvesting and storage capabilities. The post-polymerization method has proven to be advantageous for optimizing interfacial interactions and achieving superior performance compared to *in-situ* polymerization process. Characterization *via* UV-Vis, TEM, FTIR, and XPS confirms the presence of Er^{3+} ions within the composite suspension and reveals its complex interactions with PANI, PSS, and formic acid. Notably, FTIR and XPS analyses indicate that Er^{3+} ions are not directly coordinated with the PANI backbone but are instead located in the outer coordination spheres, interacting predominantly through PSS and formic acid molecules. This unique coordination facilitates energy transfer, as evidenced by the observed enhancement in photocurrent and the emergence of new redox features in CV measurements. The Er-PANI:PSS composite exhibits significantly improved electrochemical performance under light irradiation, particularly at 655 nm, achieving a 30-fold increase in current density compared to the pristine PANI:PSS suspension. This enhancement is attributed to a synergistic mechanism involving photo-assisted protonation of PANI and Er^{3+}-mediated charge storage. The Er^{3+} ions function as effective redox mediators, promoting interfacial electron transfer, stabilizing charge carriers, and generating new energy states that contribute to improved photoelectrochemical activity. LSV studies further confirm the enhanced electrochemical performance of the Er-PANI:PSS composite, highlighting its potential applicability in next-generation redox flow batteries and related energy conversion technologies. These findings establish a promising platform for the development of advanced materials capable of efficient photoelectrochemical energy harvesting and storage, with broad implications for scalable and sustainable energy systems.

Methods

Materials and chemicals

Aniline ($C_6H_5NH_2$, 99%), ammonium persulfate (APS, $(NH_4)_2S_2O_8$, 98%), poly(sodium 4-styrenesulfonate) (PSS, MW ~70 000), formic acid (HCOOH, 98%), hydrochloric acid (HCl, 35%), ethanol (C_2H_5OH, 99%), and erbium oxide (Er_2O_3, 99.9%) were purchased from Sigma-Aldrich, Czech Republic. All chemicals were used as received without further purification.

Fluorine-doped tin oxide-coated glass slides (FTO, SnO_2/F, Aldrich, 30 × 30 × 2.2 mm^3, surface resistivity 7 Ω per sq) were placed in an ultrasonic bath with acetone for 10 min, then with ethanol for 10 min and with water for 10 min. The slides were dried with N_2 flow and in vacuum oven at 60 °C/1 mbar for 4 h before using as working electrodes.

Preparation of the composite suspensions

Erbium-containing polyaniline Er-PANI:PSS suspensions were prepared *via* post-synthesis doping of PANI. PANI suspensions were initially prepared by acid-assisted polymerization as detailed in our previous work.[66] Specifically, 0.5 mL aniline diluted in 1 mL ethanol was mixed with 14.1 mL concentrated formic acid (HCOOH). Polymerization was initiated by the dropwise addition of 188 mg APS dissolved in 1 mL DI water, after PANI polymerization was completed 1 mL of PSS was introduced to stabilize the suspension, which was subsequently diluted further with PSS solution. Separately, 250 mg Er_2O_3 was dissolved in 10% HCl under controlled conditions to obtain a homogeneous solution, which was then gradually added to the PANI suspension and ultrasonicated to form Er-PANI:PSS composites.

Characterizations

UV–Vis absorption spectra of the investigated suspensions were recorded in the range of 250 to 900 nm at room temperature using a Scientific UV–Visible spectrophotometer (Evolution 220) with a 1 cm thick cuvette. Prior to the measurements, the PANI-containing suspensions were diluted to 3% of their original concentration using concentrated formic acid.

Fourier transform infrared spectra (FTIR) in region 4000–650 cm^{-1} were recorded using a Thermo Nicolet NEXUS 870 FTIR Spectrometer (MCT/A detector; 256 scans; resolution 2 cm^{-1}) equipped with GoldenGate ATR accessory. The spectra were corrected for the carbon dioxide and humidity in the optical path. Each sample solution was dropped on the ATR crystal, measured immediately, allowed to dry, and measured again.

X-ray photoelectron spectroscopy (XPS) measurements were conducted on suspensions deposited on silicon wafers using an AXIS Supra spectrometer (Kratos Analytical, U.K.).

Electrochemical and photoelectrochemical properties of the prepared liquid suspensions were investigated using a three-electrode photoelectrochemical cell (PECC-1/PECC-2) configuration, in which fluorine-doped tin oxide (FTO)-coated glass substrate was used as the working electrode, a platinum wire served as the counter electrode, and an Ag/AgCl (in 3.5 M KCl) as reference electrode. The cell was connected to an illumination system equipped with changeable LED light sources. In this study, blue (407 nm), deep red (655 nm), and white LEDs were utilized. The data were collected using an AUTOLAB PGSTAT302N potentiostat equipped with an FRA32M module, controlled *via* Nova 2.1 software. Cyclic voltammetry was conducted within a potential range of −0.3 V to 0.8 V *vs.* Ag/AgCl at a scan rate of 5 mV s^{-1}. Electrochemical impedance spectroscopy analyses were done in the frequency range from 10^5 Hz to 0.1 Hz with an amplitude of 5 mV, at an open circuit potential (OCP) of 0.50 V.

Linear sweep voltammetry (LSV) measurements were performed using a glassy carbon rotating disk electrode as the working electrode, double platinum (Pt) sheet electrode as the counter electrode, and Ag/AgCl in 3 M KCl as the reference

electrode. The measurements were conducted at different rotation speeds ranging from 200 to 3000 rpm, with a fixed scan rate of 5 mV s^{-1} over a potential range of −0.2 to 0.8 V.

Using the same configuration, electrochemical impedance spectroscopy (EIS) analyses were performed in the frequency range from 10^5 Hz to 0.1 Hz with an amplitude of 5 mV, at an open circuit potential (OCP) of 0.50 V. From the obtained CV data, the areal specific capacitance (C_s) of the investigated samples was calculated as:

$$C_s = \frac{\int I dV}{A \Delta V v}$$

where, $\int I dV$ represents the integrated area under the CV curve ($A \cdot V$), A is the electrode surface area (cm^2), ΔV refers to the potential window (V), and v is the employed scan rate (V s^{-1}).

Author contributions

The manuscript was written through contributions of all authors. All authors have given approval to the final version of the manuscript. Conceptualization (M. E., E. T.), data curation (M. E., J. S., Z. M., J. H.), formal analysis (M. E., J. S., Z. M., J. H.), funding acquisition (E. T.), investigation (M. E., J. S., Z. M., J. H., E. T.), methodology (M. E., Z. M., E. T.), project administration (E. T.), supervision (E. T.), validation (M. E., J. S., Z. M., J. H.), visualization (M. E., J. S., Z. M., J. H.), writing – original draft (M. E., Z. M., E. T.), writing – review & editing (M. E., E. T.).

Conflicts of interest

There are no conflicts to declare.

Data availability

The data described in the manuscript are available from the SI and corresponding authors. Supplementary information is available. EIS of Er-PANI:PSS; TEM and EDX analysis of Er-PANI:PSS composite; XPS Survey spectra; Evolution of the peak current of Er-PANI:PSS; SEM images and corresponding EDX data of films deposited on FTO; Limiting current vs square root of scat rates; EIS data and corresponding equivalent circuit fitting curves; Areal capacitance of different systems, calculated from CV. See DOI: https://doi.org/10.1039/d5nr02298c.

Acknowledgements

References

1 Events - IEA. https://www.iea.org/events.

2 H. Adeh, S. P. Good, M. Calaf and C. W. Higgins, Solar pV power potential is Greatest over croplands, *Nat. Sci. Rep.*, 2019, **9**, 11442.

3 B. Luo, Recent Progress on Integrated Energy Conversion and Storage Systems, *Adv. Sci.*, 2017, **4**, 1700104.

4 Y. Lu, M. Chen, G. Zhu and Y. Zhang, Recent progress in the study of integrated solar cell-energy storage systems, *Nanoscale*, 2024, **16**, 8778–8790.

5 V. A. Savekar, *et al.*, Bridging energy harvesting and storage through self-charging photo-supercapacitors: Achievements, innovations, challenges, and future horizons, *J. Energy Storage*, 2025, **111**, 115366.

6 H. Liu, *et al.*, Porous tremella-like MoS2/polyaniline hybrid composite with enhanced performance for lithium-ion battery anodes, *Electrochim. Acta*, 2015, **167**, 132–138.

7 H. E. Katz, P. C. Searson and T. O. Poehler, Batteries and charge storage devices based on electronically conducting polymers, *J. Mater. Res.*, 2010, **25**, 1561–1574.

8 G. A. Snook, P. Kao and A. S. Best, Conducting-polymer-based supercapacitor devices and electrodes, *J. Power Sources*, 2011, **196**, 1–12.

9 S. Tajik, Recent developments in conducting polymers: applications for electrochemistry, *RSC Adv.*, 2020, **10**, 37834–37856.

10 Z. Li and L. Gong, Progress on Applications of Polyaniline (PANI) for Electrochemical Energy Storage and Conversion, *Materials*, 2020, **13**, 548.

11 M. Beygisangchin, Preparations, Properties, and Applications of Polyaniline and Polyaniline Thin Films-A Review, *Polymers*, 2021, **13**, 2003.

12 S. Bhadra, D. Khastgir, N. K. Singha and J. H. Lee, Progress in preparation, processing and applications of polyaniline, *Prog. Polym. Sci.*, 2009, **34**, 783–810.

13 E. Tomšík, Enhanced Electrochemical Performance of Polyaniline-Boron Doped Diamond Electrode for Supercapacitor Applications, *Small Methods*, 2025, **9**, 2401523.

14 P. C. Dent, Rare earth elements and permanent magnets (invited), *J. Appl. Phys.*, 2012, **111**, 07A721.

15 B. Yang, *et al.*, Effect of lanthanum, cerium and other elements on the electrochemical corrosion properties of Pb–Ca–Sn–Al alloy in lead–acid batteries, *J. Energy Storage*, 2019, **25**, 100908.

16 W. Zhang, *et al.*, The effect of rare earth metals on the microstructure and electrochemical corrosion behavior of lead calcium grid alloys in sulfuric acid solution, *J. Power Sources*, 2012, **203**, 145–152.

17 S. L. Lin, *et al.*, Characterization of spent nickel–metal hydride batteries and a preliminary economic evaluation of the recovery processes, *J. Air Waste Manage. Assoc.*, 2016, **66**, 296–306.

18 H. Zhao, *et al.*, Rare earth incorporated electrode materials for advanced energy storage, *Coord. Chem. Rev.*, 2019, **390**, 32–49.

19 D. Zeng, et al., A high-performance aqueous Eu/Ce redox flow battery for large-scale energy storage application, Int. J. Heat Mass Transfer, 2024, 233, 125978.

20 Y. Wu, et al., A green europium-cerium redox flow battery with ultrahigh voltage and high performance, Chem. Eng. J., 2024, 500, 157189.

21 K. Chen and D. Xue, Formation of electroactive colloids via in situ coprecipitation under electric field: Erbium chloride alkaline aqueous pseudocapacitor, J. Colloid Interface Sci., 2014, 430, 265–271.

22 M. Elrouby, A. M. Abu-Dief and I. M. A. Mohamed, Facile synthesis and electrochemical characterization of erbium oxide and hydroxide for supercapacitor applications, Ionics, 2024, 30, 5699–5711.

23 S. Liu, Er-Doped $LiNi_{0.5}Mn_{1.5}O_4$ Cathode Material with Enhanced Cycling Stability for Lithium-Ion Batteries, Materials, 2017, 10, 859.

24 M. S. Waheed, et al., Fabrication of mesoporous Er doped ZnMnO3 nanoflake via sol gel approach for energy storage application, Ceram. Int., 2023, 49, 13298–13309.

25 J. Stejskal, P. Kratochvíl and N. Radhakrishnan, Polyaniline dispersions 2. UV—Vis absorption spectra, Synth. Met., 1993, 61, 225–231.

26 I. M. Minisy, Z. Morávková, J. Hromádková and P. Bober, Conductive films cast from highly stable PEDOT and PEDOT/silver colloidal dispersions, Prog. Org. Coat., 2025, 201, 109113.

27 H. R. Tantawy, A. T. Weakley and D. E. Aston, Chemical effects of a solvent-limited approach to hcl-doped polyaniline nanopowder synthesis, J. Phys. Chem. C, 2014, 118, 1294–1305.

28 A. Watanabe, K. Mori, Y. Iwasaki, Y. Nakamura and S. Niizuma, Electrochromism of Polyaniline Film Prepared by Electrochemical Polymerization, Macromolecules, 1987, 20, 1793–1796.

29 A. Gruger, A. El Khalki and P. Colomban, Protonation, sol formation and precipitation of poly-and oligoanilines, J. Raman Spectrosc., 2003, 34, 438–450.

30 H. J. Salavagione, D. F. Acevedo, M. C. Miras, A. J. Motheo and C. A. Barbero, Comparative Study of 2-Amino and 3-Aminobenzoic Acid Copolymerization with Aniline Synthesis and Copolymer Properties, J. Polym. Sci., Part A: Polym. Chem., 2004, 42, 5587–5599.

31 S. Folch, A. Gruger, A. Régis and P. Colomban, Optical and vibrational spectra of sols/solutions of polyaniline: water as secondary dopant, Synth. Met., 1996, 81, 221–225.

32 B. J. Holliday and T. M. Swager, Conducting metallopolymers: the roles of molecular architecture and redox matching, Chem. Commun., 2005, 1, 23–36.

33 J. Han, M. Wang, Y. Hu, C. Zhou and R. Guo, Conducting polymer-noble metal nanoparticle hybrids: Synthesis mechanism application, Prog. Polym. Sci., 2017, 70, 52–91.

34 H. J. Kim, et al., Fabrication of Nanocomposites Complexed with Gold Nanoparticles on Polyaniline and Application to Their Nerve Regeneration, Cite This, ACS Appl. Mater. Interfaces, 2020, 12, 30760.

35 S. K. Filippov, et al., Dynamic light scattering and transmission electron microscopy in drug delivery: a roadmap for correct characterization of nanoparticles and interpretation of results, Mater. Horiz., 2023, 10, 5354–5370.

36 K. Okada, Y. Kaizu and H. Kobayashi, Aqualigand dissociation of 5d←4f excited $[Ce(OH2)9]3+$ in aqueous solution, J. Chem. Phys., 1981, 75, 1577–1578.

37 M. K. Bera, et al., 8734–8745 Downloaded via LIBRARY OF CZECH ACADEMY OF SCIENCES on April 23, J. Phys. Chem. B, 2015, 119, 17.

38 E. Fernández-Ramírez, M. Jiménez-Reyes and M. J. Solache-Ríos, Effects of Ionic Strength and Charge Density on the Stability of Chloride Complexes of Trivalent Lanthanides, J. Chem. Eng. Data, 2008, 53, 1756–1761.

39 W. Rudolph and G. Irmer, On the Hydration of Heavy Rare Earth Ions: Ho^{3+}, Er^{3+}, Tm^{3+}, Yb^{3+} and Lu^{3+}—A Raman Study, Molecules, 2019, 24, 953.

40 L. Soderholm, S. Skanthakumar and R. E. Wilson, Structures and Energetics of Erbium Chloride Complexes in Aqueous Solution, J. Phys. Chem. A, 2009, 113, 6391–6397.

41 A. Habenschuss and F. H. Spedding, The coordination (hydration) of rare earth ions in aqueous chloride solutions from x ray diffraction. I.TbCl3,DyCl3, ErCl3,TmCl3,and LuCl3, J. Chem. Phys., 1979, 70, 2797–2806.

42 E. J. Graeber, G. H. Conrad and S.-W. F. Duliere, Crystallographic data for solvated rare earth chlorides. 1012 SHORT Commun, Acta Crystallogr., 1966, 21, 1012.

43 Z. Ahmed, Near infrared organic light emitting devices based on a new erbium(III) β-diketonate complex: synthesis and optoelectronic investigations, RSC Adv., 2017, 7, 18239–18251.

44 D. A. Long, Infrared and Raman characteristich group frequencies. Tables and charts George Socrates John Wiley and Sons, Ltd, Chichester, Third Edition, 2001. Price £135, J. Raman Spectrosc., 2004, 35, 905–905.

45 S. Dasari, Z. Abbas, P. Kumar and A. K. Patra, From chip-in-a-lab to lab-on-a-chip: towards a single handheld electronic system for multiple application-specific lab-on-a-chip (ASLOC), Lab Chip, 2014, 14, 2168–2176.

46 S. Destri, W. Porzio, F. Meinardi, R. Tubino and G. Salerno, Novel erbium-substituted oligothiophene chelates for infrared emission, Macromolecules, 2003, 138, 289–293.

47 Z. Ahmed, K. Mahiya and K. Iftikhar, Cite this, New J. Chem., 2020, 44, 13172.

48 R. Janicki and A. Mondry, A new approach to determination of hydration equilibria constants for the case of [Er(EDTA)(H 2 O) n] À complexes † Two anionic complexes [Er(EDTA)(H 2 O) 2] À and [Er(EDTA)(H 2 O) 3] À were obtained in the form of the following compounds: [C(NH 2) 3] 2 [Er(EDTA)(H 2 O) 2]ClO 4 Á6H 2 O (I) and Na[Er (EDTA)(H 2 O) 3]Á5H 2 O (II), respectively, Phys. Chem. Chem. Phys., 2014, 16, 26823.

49 J. Stejskal, M. Trchová and T. Trchová, Aniline oligomers versus polyaniline, Polym. Int., 2012, 61, 240–251.

50 M. Trchová, I. Sapurina, J. Prokeš and J. Stejskal, FTIR spectroscopy of ordered polyaniline films, *Synth. Met.*, 2003, **135–136**, 305–306.

51 B. Golesorkhi, *et al.*, Ligand-Sensitized Near-Infrared to Visible Linear Light Upconversion in a Discrete Molecular Erbium Complex, *J. Am. Chem. Soc.*, 2021, **143**, 15326–15334.

52 S. Bo, J. Hu, Q. Wang, X. Liu and Z. Zhen, Near-infrared luminescence properties of erbium complexes with the substituted phthalocyaninato ligands, *Photochem. Photobiol. Sci.*, 2008, **7**, 474–479.

53 M. A. Bekhti, Enhanced tailored of thermal stability, optical and electrochemical properties of PANI matrix containing Al_2O_3 hybrid materials synthesized through in situ polymerization, *Polym. Compos.*, 2021, **42**, 6–14.

54 M. Šetka, Raman and Xps studies of ammonia sensitive polypyrrole nanorods and nanoparticles, *Sci Rep*, 2019, **9**, 8465.

55 S. Cho, J. S. Lee, J. Jun, S. G. Kim and J. Jang, Fabrication of water-dispersible and highly conductive PSS-doped PANI/graphene nanocomposites using a high-molecular weight PSS dopant and their application in H2S detection, *Nanoscale*, 2014, **6**, 15181–15195.

56 R. Morarad, W. Naeowong and A. Sirivat, Iontophoretically controlled insulin delivery via water-soluble conductive polymer PANI:PSS and thermoplastic polyurethane matrix, *Drug Deliv. Transl. Res.*, 2024, **14**, 280–293.

57 Y. Yang, *et al.*, Visible-light driven photocatalyzing degradation of antibiotics and dyes enabled by 0D/1D Tb2O3/Er2O3/TiO2@C hybrids, *Mater. Res. Bull.*, 2024, **178**, 112910.

58 L. Li, *et al.*, Preparation of a novel Ti/TNAs/PbO2-PVDF-Er2O3 anode by Ti3 + self-doping TNAs and its electrocatalytic performance for hydroquinone degradation, *J. Environ. Chem. Eng.*, 2023, **11**, 110379.

59 S. Bouallag, A. Mougari, M. Zabat and A. Belayadi, Computational study of transition metal coordinated polyaniline: A first principle investigation into tuning the electronic properties of the resulting hybrid material, *Physica B: Condens. Matter*, 2024, **695**, 416597.

60 A. Franco-Cañellas, S. Duhm, A. Gerlach and F. Schreiber, Binding and electronic level alignment of π-conjugated systems on metals, *Rep. Prog. Phys.*, 2020, **83**, 066501.

61 T. P. Silverstein, Marcus Theory: Thermodynamics CAN Control the Kinetics of Electron Transfer Reactions, J. Chem. Educ., 2012, **89**, 1159–1167.

62 E. Zanzola, *et al.*, Redox Solid Energy Boosters for Flow Batteries: Polyaniline as a Case Study, *Electrochim. Acta*, 2017, **235**, 664–671.

63 Y. Itabashi, H. Asahara and K. Ohkubo, Chlorine-radical-mediated C-H oxygenation reaction under light irradiation, *Chem. Commun.*, 2023, **59**, 7506–7517.

64 J. Barichello, P. Mariani, L. Vesce, D. Spadaro, I. Citro, F. Matteocci, A. Bartolotta, A. Di Carlo and G. Calogero, Bifacial dye-sensitized solar cells for indoor and outdoor renewable energy-based application, *J. Mater. Chem. C*, 2024, **12**, 2317–2349.

65 N. Sinha, C. Wegeberg, D. Haussinger, A. Prescimone and O. Wenger, Photoredox-active Cr(O) limunophores featuring photophysical properties competitive with Ru(ɪɪ) and Os(ɪɪ) complexes, *Nat. Chem.*, 2023, **15**, 1730–1736.

66 E. Tomšík, A New Method to Prepare Stable Polyaniline Dispersions for Highly Loaded Cathodes of All-Polymer Li-Ion Batteries, *Polym.*, 2023, **15**, 2508.